Available online at www.sciencedirect.com
SCIENCE DIRECT®
Journal of Computational Physics 189 (2003) 212–238
JOURNAL OF COMPUTATIONAL PHYSICS
www.elsevier.com/locate/jcp

Incorporation of lubrication effects into the force-coupling method for particulate two-phase flow

S.L. Dance *, M.R. Maxey

Division of Applied Mathematics, Brown University, Providence, RI 02912, USA

Received 1 March 2002; received in revised form 8 March 2003; accepted 19 March 2003

Abstract

We investigate the performance of the force-coupling method (FCM) for particulate flow at microscales. In this work, we restrict attention to flows where we may neglect fluid inertia (Stokes flows), particle inertia and Brownian motion. The FCM performs well when distances between solid boundaries are sufficiently large, however it does not capture the local effects of viscous lubrication forces for small gap widths. To improve the results, we develop a parameterization of the lubrication forces for inclusion in the model. This is based on exact results for isolated pairs of particles and single particle–wall configurations. The correction is imposed through the addition of a lubrication barrier force on affected particles. The parameterization is tested for several cases, illustrating both the improvements possible and the limitations.

Keywords: Lubrication forces; Two-phase flow

1. Introduction

The sedimentation of particles in a liquid is a classical fluid mechanics problem. One of the major issues in modeling such a system is the disparity between the lengthscales of the fluid flow, typically of the order of the size of the fluid container ($\sim 10^{-1}$ m), and the small size of the particles themselves ($\sim 10^{-4}$ m). As a consequence, most commonly used methods fall into one of two categories: those that achieve macroscopic results for bulk quantities, at the expense of accurate modeling of microscopic effects; and those that model the small scale effects accurately, but are limited in the number of particles they can handle.

There are various methods available for simulating suspension flows. Hu [19] and Johnson and Tezduyar [27] have developed finite element methods which accommodate moving boundaries and fully resolve the flow. Another approach which uses a fixed grid is the distributed Lagrange multiplier (DLM) method [16].

* Corresponding author. Present address: Meteorology Department, University of Reading, Earley Gate, P.O. Box 243, Reading RG6 6BB, UK.
E-mail address: dance@cfm.brown.edu (S.L. Dance).

0021-9991/03/$ - see front matter
doi:10.1016/S0021-9991(03)00209-2

This has been employed for moderate particle Reynolds numbers, and non-Newtonian flows. Immersed boundary schemes have been applied to Stokes suspensions [11,46]. A Lattice–Boltzmann model has been utilized by Ladd and co-workers (see [30] for a review).

Some methods employ the special properties of Stokes flows. The boundary integral technique falls into this category (see [22,40] for examples of boundary integral methods for multiparticle systems). There are also methods based on multipole expansion techniques, e.g. [43]. Stokesian Dynamics [3] is a widely used multipole method. Various improvements to Stokesian Dynamics have recently been published, including the implementation of a fast multipole technique for calculation of the mobility matrix [20], the use of iterative methods for inversion of the mobility matrix [21] and the use of particle-mesh Ewald summation techniques and fast Fourier transforms in periodic geometries [44].

This paper is concerned with making microscale improvements to the Force-Coupling Method (FCM). The FCM is described in [34,37]. Validation of the method for Stokes flows is given in [33,37] for various geometries. The method is also appropriate for $0 < Re_p < 20$. ($Re_p = 2aU/v$, where a is the particle radius, U is the particle velocity and v is the kinematic viscosity of the fluid.) Comparisons with direct numerical simulations at finite Re_p are given in [32]. Comparisons with experiments are described in [33,35].

Some of the computational advantages of the FCM include:

- The flow domain is covered with a fixed mesh – there is no need to re-grid as the particles move around the domain.
- The method is suitable for use in complex geometries and may be incorporated in standard flow solvers.
- High-order spectral methods may be used to solve for the flow, since the particles are distributed using smooth Gaussian envelopes.
- We have low spatial resolution requirements within each particle.
- Modeling large numbers of particles ($O(10^6)$) is well within current computational capability.

The model extends to ellipsoidal particles via a simple rescaling of the particle envelope [33]. Preliminary results for finite Re_p flows past ellipsoidal particles show good agreement between the FCM and DNS [31].

Maxey and Patel [37] showed that the FCM reproduces the flow past an isolated sphere quite well, agreeing with the true solution at distances greater than $1/4a$ away from the particle surface. Closer to the particle surface, the flow is smoothed out. Lomholt and Maxey [34] extended the analysis of particle pair configurations and considered horizontal channel geometries. For particles close to, and in relative motion with, another solid boundary, they found that the FCM underestimates the hydrodynamic drag. The use of force-dipole terms improved the flow description and accuracy of particle velocities, for near–wall interactions, or when particles were close together. The results given here show that nevertheless, when the spacing is very small, only a limited accuracy can be attained.

Particles close to, and in relative motion with a rigid boundary (such as a wall or another particle) induce a hydrodynamic force that acts to retard the motion of the particles. If a is the characteristic length scale of the particle, and $a\epsilon$ is the smallest separation distance between the two boundaries, an asymptotic calculation for Stokes flow shows that at leading order, for a fixed relative velocity, the drag on the particle is singular in the small parameter ϵ. This can create difficulties when computing numerical solutions. In principle, with infinite resolution, lubrication forces would be sufficient to prevent particles colliding in inertia-less Stokes flow. In practice, to avoid expensive asynchronous time-step reduction, a repulsive force barrier is often employed to avoid overlap of particles.

The main goal of this work is to show how lubrication effects may be incorporated into the FCM scheme and illustrate the contexts in which they are important. The parameterization is based on exact results for isolated pairs of particles and particle–wall configurations at $Re_p = 0$, and known results for the FCM. The correction is imposed through the addition of a lubrication barrier force on affected particles. The main improvements are seen in the particle velocities. Results are presented showing situations where there is good agreement between the lubrication-augmented FCM model and exact results, as well as contexts where the accuracy of the model is limited by the use of pairwise and particle–wall estimates in its formulation.

Throughout this article, particles are assumed to be identical smooth rigid spheres. The effects of surface roughness [47] and electrostatic repulsion between particles with polymer coats [42] are neglected. In addition, we restrict to flows where fluid inertia, particle inertia and Brownian motion may be neglected. For example, this would be appropriate for the sedimentation of non-colloidal particles, where particle accelerations are small relative to gravity. At finite Re_p the experimental results of Gondret et al. [18] and numerical results of Lomholt [33] have shown that lubrication forces are less important, or act only over shorter distances.

The paper is organized as follows: The FCM is described briefly in Section 2. In Section 3 we review asymptotic results for particle pairs and particle–wall configurations where the lubrication approximation is relevant. We give a few example comparisons of FCM simulations with these results. These demonstrate the need for the inclusion of a lubrication correction. In Section 4, we describe our implementation of a lubrication parameterization. Example simulations using the parameterization are presented in Section 5. We conclude in Section 6. Appendices provide documentation of a novel iteration scheme for calculating FCM-dipole terms, and an implementation of the Uzawa scheme with the FCM for Stokes flows.

2. The force-coupling model

In this section we give a brief overview of the FCM. The reader is referred to the descriptions in [34,37] for further details. Additional material may be found in [33].

2.1. Model description

The FCM is defined on a domain $(\mathbf{x},t) \in \Omega \times \mathbb{R}$, $\Omega \subseteq \mathbb{R}^3$. The fluid is assumed to extend over the whole domain, including the volume occupied by the particles. The fluid velocity field, $\mathbf{u}(\mathbf{x},t)$, and pressure, $p(\mathbf{x},t)$, satisfy the Stokes equations:

$$-\mu\nabla^2\mathbf{u} + \nabla p = \mathbf{f}, \tag{1}$$

$$-\nabla \cdot \mathbf{u} = 0 \tag{2}$$

in $(\mathbf{x},t) \in \Omega \times \mathbb{R}$, where μ is the dynamic viscosity of the fluid. The flow must also satisfy prescribed boundary conditions, specified according to the geometry of the problem (e.g., periodic boundary conditions, no-slip (Dirichlet) conditions, etc.) We do not impose boundary conditions on the particle surfaces. In contrast to a true multipole method, which uses the boundary conditions on the particle surfaces to calculate the multipole strengths, the FCM imposes constraints on volume averaged moments of the flow, which are consistent with the presence of a rigid particle. These are explained below.

The fluid momentum Eq. (1) is augmented with a source term, $\mathbf{f}(\mathbf{x},t)$, which approximates the effect of the particles on the flow, using FCM-multipole terms:

$$f_i(\mathbf{x},t) = \sum_{n=1}^{N} F_i^{(n)} \Delta^{(n)}(\mathbf{x} - \mathbf{Y}^{(n)}(t)) + G_{ij}^{(n)} \frac{\partial \Theta^{(n)}}{\partial x_j}(\mathbf{x} - \mathbf{Y}^{(n)}(t)). \tag{3}$$

The sum is over all the particles in the system, the nth particle being located at $\mathbf{Y}^{(n)}(t)$. The first term in the sum is known as the force-monopole and the second as the force-dipole: these are the FCM equivalents of their namesakes in the multipole expansion. The functions $\Delta^{(n)}(\mathbf{x})$ and $\Theta^{(n)}(\mathbf{x})$ are spherically symmetric Gaussian functions which we may think of as finite analogies of a Dirac delta function:

$$\Delta^{(n)}(\mathbf{x}) = \frac{1}{\left(2\pi\sigma_{\Delta,n}^2\right)^{3/2}} \exp\left(\frac{-\mathbf{x}^2}{2\sigma_{\Delta,n}^2}\right) \tag{4}$$

$$\Theta^{(n)}(\mathbf{x}) = \frac{1}{\left(2\pi\sigma_{\Theta,n}^2\right)^{3/2}} \exp\left(\frac{-\mathbf{x}^2}{2\sigma_{\Theta,n}^2}\right), \tag{5}$$

where $\sigma_{\Delta,n}$ and $\sigma_{\Theta,n}$ are lengthscales related to the particle radius, a_n. Their values are calculated by matching particle velocities obtained with the FCM to exact solutions for an isolated particle, settling in a quiescent fluid and in a pure straining flow, respectively. This results in $\sigma_{\Delta,n} = a_n/\pi^{1/2}$ and $\sigma_{\Theta,n} = a_n/(36\pi)^{1/6}$. For further details, see [34,37].

Initial positions for each particle are prescribed. Particle positions evolve as

$$\frac{\mathrm{d}Y_i^{(n)}}{\mathrm{d}t} = V_i^{(n)}. \tag{6}$$

The particle velocities are computed as a local average of the fluid velocity:

$$V_i^{(n)}(t) = \int u_i(\mathbf{x},t)\Delta^{(n)}(\mathbf{x} - \mathbf{Y}^{(n)}(t))\,\mathrm{d}^3\mathbf{x}. \tag{7}$$

With this definition for the velocity, we find a consistent energy balance between the rate of working by the particulate phase and viscous dissipation of kinetic energy by the fluid [37]. The particle angular velocity is given by

$$\Omega_i^{(n)}(t) = \frac{1}{2}\int \omega_i(\mathbf{x},t)\Theta^{(n)}(\mathbf{x} - \mathbf{Y}^{(n)}(t))\,\mathrm{d}^3\mathbf{x}, \tag{8}$$

where ω is the local fluid vorticity. The motivation for this definition is given in [33].

2.2. Calculating the multipole strengths

The force-monopole strength, $\mathbf{F}^{(n)}$, is equal to the hydrodynamic drag on the nth particle. Typically, this is equal to the buoyancy adjusted weight of the particle, minus the particle inertia:

$$\mathbf{F}^{(n)} = (m_\mathrm{p} - m_\mathrm{f})\left(\mathbf{g} - \frac{\mathrm{d}\mathbf{V}^{(n)}}{\mathrm{d}t}\right).$$

In this work we neglect particle inertia. This is appropriate for sedimenting suspensions where the effect of gravitational acceleration is much larger than accelerations in the fluid.

The force-dipole strength tensor, $G_{ij}^{(n)}$ may be split into a symmetric part, $S_{ij}^{(n)}$ and an antisymmetric part, $A_{ij}^{(n)}$, such that $G_{ij}^{(n)} = S_{ij}^{(n)} + A_{ij}^{(n)}$. The antisymmetric part is related to the external torque on the particle, $\mathbf{T}^{(n)}$, via $A_{ij}^{(n)} = \frac{1}{2}\varepsilon_{ijk}T_k^{(n)}$.

The symmetric part, the stresslet, is related to the rate of strain tensor, given by $e_{ij} = \frac{1}{2}(\partial u_i/\partial x_j + \partial u_j/\partial x_j)$. Since we have rigid particles which may not deform, we require that, on the average, we have zero rate of strain within the particle

$$E_{ij}^{(n)} = \int e_{ij}(\mathbf{x})\Theta^{(n)}(\mathbf{x} - \mathbf{Y}^{(n)})\,\mathrm{d}^3\mathbf{x} = 0. \tag{9}$$

With this definition of $E_{ij}^{(n)}$, the constraint also implies that there is no work done by the stresslet. The exact computation of $S_{ij}^{(n)}$ involves the construction and solution of a $5N \times 5N$ linear system:

$$\mathscr{L}\mathscr{S} = \mathscr{E},$$

where $\mathscr{L}$ represents the FCM Stokes flow operator which maps stresslet strengths to averaged particle strains. $\mathscr{L}$ is a linear operator which depends on the geometry of the system and the particle positions. $\mathscr{S}$ is the unknown, containing the independent components of the stresslet for each particle. $\mathscr{E}$ is the $5N$ vector containing all the independent elements of the strain for each particle, determined from the flow due to the external forces and torques on each particle. An iterative method is used to compute the solution. This avoids assembling the operator $\mathscr{L}$. The reader is directed to Appendix A for details of a novel scheme employed for this calculation. This method gives faster convergence than the scheme described by Lomholt [33].

In subsequent sections we will illustrate the effect of the inclusion or omission of the dipole term using example simulations.

3. Lubrication effects

The work of Lomholt and Maxey [34] showed that the FCM smoothes the flow field in the regions close to particle surfaces. Hence, the FCM underestimates the hydrodynamic drag on particles in close approach to another boundary. Such underestimation can lead to unphysical effects such as particle overlap. In FCM simulations of random suspensions by Climent and Maxey [6], such overlaps were prevented using a collision barrier. This consisted of a repulsive potential force which was added to the force monopole on particles sufficiently close to another solid boundary. The functional form of the force was chosen for convenience, and the effects on the bulk flow assumed small. The potential force barrier is given in Appendix B. The DLM method also uses a repulsive force formulation to prevent collisions. This is described in [16].

In this section, we briefly review the asymptotic results of lubrication theory for a single sphere close to a plane wall, and for isolated pairs of particles. We present some examples of the failure of the FCM to resolve these effects for the case of a single-sphere and a plane wall. Similar results for isolated pairs of spheres are presented in [34]. We extend the idea of parameterizing microscale effects in the FCM such that the parameterization has a basis in lubrication theory. It is worth noting that with a fixed time-step, hydrodynamic effects alone are insufficient to prevent overlap in all cases, so in dynamic simulations we must also include a repulsive force, to act at the smallest scales. Dratler and Schowalter [10] found that Stokesian Dynamics, which resolves pairwise lubrication effects, also needs some form of repulsive force in order to prevent overlaps between particles.

3.1. Particle–wall interactions

3.1.1. Asymptotic results

For a single particle in a Stokes flow there is a linear relation between the velocity of the particle, and the force and torque on it:

$$F_i = 6\pi\mu a\left(\mathscr{A}_{ij}U_j + a\mathscr{B}_{ij}\Omega_j\right), \tag{10}$$

$$T_i = 8\pi\mu a^2\left(\mathscr{C}_{ij}U_j + a\mathscr{D}_{ij}\Omega_j\right). \tag{11}$$

$\mathscr{A}, \mathscr{B}, \mathscr{C}, \mathscr{D}$ are dimensionless second rank tensors whose values are solely dependent on the geometry. The Lorentz reciprocal theorem for the homogeneous Stokes equations implies that $\mathscr{A} = \mathscr{A}^{\mathrm{T}}$, $\mathscr{D} = \mathscr{D}^{\mathrm{T}}$ and $\mathscr{B}^{\mathrm{T}} = \mathscr{C}$, for any geometry. It is worth noting that the reciprocal theorem also holds for the FCM.

We refer to right-handed orthonormal axes with the $\mathbf{e}_1$ direction normal to the wall and the other directions parallel to the wall (see Fig. 1). Symmetry considerations imply that with respect to these axes $\mathscr{A}$ is diagonal, and $\mathscr{A}_{22} = \mathscr{A}_{33}$. The only non-zero elements of $\mathscr{B}$ are $\mathscr{B}_{23} = -\mathscr{B}_{32}$. We may use the reciprocal theorem to calculate $\mathscr{C}$ from $\mathscr{B}$. $\mathscr{D}$ is diagonal, and $\mathscr{D}_{22} = \mathscr{D}_{33}$.

The calculation of the tensors $\mathscr{A}, \mathscr{B}, \mathscr{C}, \mathscr{D}$ is referred to as a resistance problem. For a given distance between the particle and the wall, their non-zero-entries may be computed from the solutions for four configurations with prescribed velocities. Fig. 2 illustrates three of these configurations. Setting the velocities in the figure as $U_1 = -U$, $U_2 = 0$, $\Omega_3 = 0$ gives a squeezing flow. This arrangement of the particle and wall may be used to calculate the component $\mathscr{A}_{11}$ in the resistance matrix. $U_1 = 0$, $U_2 = U$, $\Omega_3 = 0$ corresponds to a translational shearing flow. This configuration may be used to calculate the components $\mathscr{A}_{22}$ and $\mathscr{C}_{32}$ in the resistance matrix. $\mathscr{B}_{23}$ follows by reciprocity. A rotational shearing flow, $U_1 = 0$, $U_2 = 0$, $\Omega_3 = \Omega$, may be used to calculate $\mathscr{D}_{33}$ and $\mathscr{B}_{23}$ directly. $\mathscr{D}_{11}$ can be calculated from an arrangement of a sphere rotating with angular velocity Ω about a normal to the wall (not illustrated).

For each component the dominant contributions may be determined using an asymptotic expansion in the small parameter ϵ, the non-dimensional gap-width. These expressions are published in the literature, unfortunately with many minor typographical errors. In Table 1 we give asymptotic series in a standardized notation, resulting from careful cross-checking of results (and in some cases derivations) from the listed references. Note that the inner solutions are singular (except for $\mathscr{D}_{11}$). These inner solutions may require an O(1) correction, which in practice is obtained by fitting to numerical data. With the exception of the $\mathscr{D}_{11}$ term, the O(1) results given in the table are calculated as the $\epsilon = 0$ limit of a linear least-squares fit of the exact data given in the listed references (for $\epsilon \leqslant 0.1$). For the case of $\mathscr{D}_{11}$ the O(1) correction is known in closed form [25].

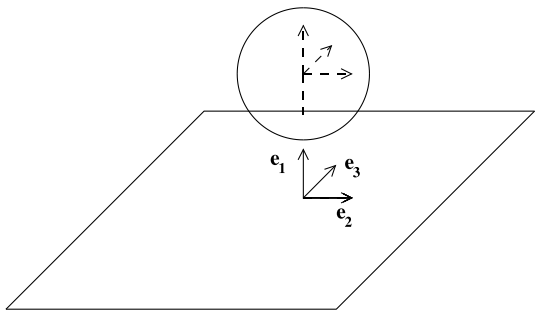

Fig. 1. Particle–wall axes.

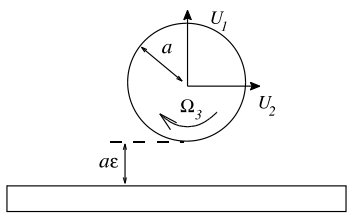

Fig. 2. Sphere and wall configurations.

Table 1
Lubrication theory results and O(1) corrections for a sphere moving close to a wall

		Inner solution		O(1)			References
$\mathscr{A}_{11}$	=	$-\frac{1}{\epsilon}+\frac{1}{5}\log\epsilon+\frac{1}{21}\epsilon\log\epsilon$	+	−0.848	+	$O(\epsilon)$	[4,8,23,29]
$\mathscr{A}_{22}$	=	$\frac{8}{15}\log\epsilon+\frac{64}{375}\epsilon\log\epsilon$	+	−0.952	+	$O(\epsilon)$	[17,25,29,39]
$\mathscr{B}_{23}$	=	$-\frac{2}{15}\log\epsilon-\frac{86}{375}\epsilon\log\epsilon$	+	−0.257	+	$O(\epsilon)$	[7,17,25,29]
$\mathscr{D}_{11}$	=	$\frac{1}{2}\epsilon\log\epsilon$	+	−1.202	+	$O(\epsilon)$	[25,26]
$\mathscr{D}_{33}$	=	$\frac{2}{5}\log\epsilon+\frac{66}{125}\epsilon\log\epsilon$	+	−0.371	+	$O(\epsilon)$	[7,17,25,29]

3.1.2. FCM results

We solve the FCM equations in a channel, using the Uzawa algorithm with a mixed Fourier-spectral element discretization. The code is described in Appendix C. A single particle, of radius $a = 1$ is placed in the channel, with an imposed force of $6\pi\mu a$ acting on it. This corresponds to the Stokes drag on an isolated sphere moving at a velocity of 1.0. The fluid viscosity, $\mu = 1$. The dimensions of the channel were chosen to be $20a$ in the wall normal direction, and $50a$ in each periodic direction, in order to diminish the effect of the periodic boundary conditions and the upper wall. The spatial resolution is 67 points in the wall normal direction and 160 in the periodic directions.

It should be noted that the FCM is set up to solve mobility problems. In other words, given a force and torque on each particle, the FCM will compute the particle velocities. This is the inverse of the resistance calculations described in the previous section. The mobility problem perhaps presents a more natural perspective, since experimentally we may specify a force or torque on a particle (via for example gravity or electromagnetic fields), but we may not specify a velocity. Here, we only consider imposed forces, since we are ultimately interested in sedimentation problems.

Imposed force normal to the wall. We impose a force on the sphere, normal to the wall, and it translates in the direction of the force without rotating. This is analogous to the flow in Fig. 2, with $U_1 = -U$, $U_2 = 0$, $\Omega_3 = 0$. The hydrodynamic drag on the particle is equal and opposite to the imposed force. Utilizing Eq. (10) we see that the ratio between the imposed force and the computed velocity should be

$$\frac{F_1}{6\pi\mu a U} = -\mathscr{A}_{11}, \tag{12}$$

where the leading order term from Table 1 is $O(\epsilon^{-1})$. In Fig. 3 we compare results from the FCM with exact results. Away from the wall, the FCM matches the exact data and there is negligible difference between the results using just the force-monopole term and those which include the force-dipole term. As ϵ is decreased the simulations with and without the dipole term diverge. When $\epsilon = 0$, the ratio $F_1/(6\pi\mu a U_1)$ takes on finite values, namely 4.38 and 7.77 for the simulation using the force-monopole term alone and that which includes the force-dipole correction, respectively. In the exact solution the particle is brought to rest when it touches the wall, illustrating that $\epsilon \to 0$ is indeed a singular limit. The FCM data has been fitted to a polynomial function of ϵ, given in Appendix D.

The difference between the velocity fields for the two FCM simulations is made evident by Fig. 4 in which a sphere sediments towards a wall. Panel (a) shows a simulation using both monopole and dipole terms. The computed flow using just the monopole term is illustrated in (b). The circle indicates the position of each sphere, the sphere center being located $1.01a$ away from the wall. The plots are in frames in which the sphere is at rest. Note that the configuration is axisymmetric. In both cases the flow is smoothed out close to the particle, and the forward stagnation point is shifted away from the wall. In the case where the force-dipole terms are included, the virtual sphere (region of closed streamlines) is enclosed within the

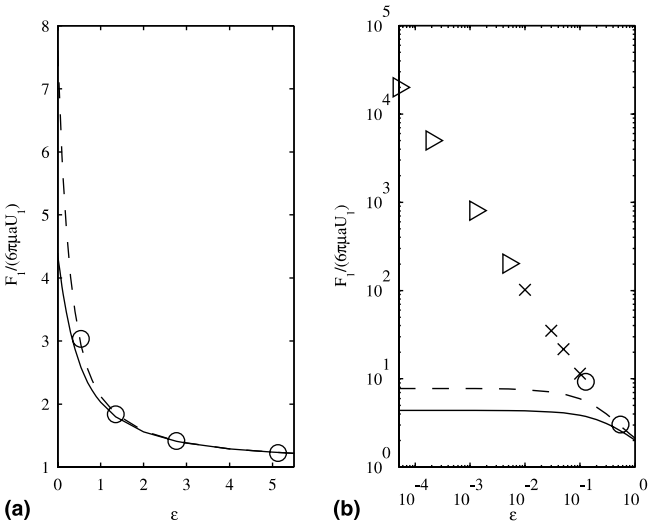

Fig. 3. (a) Linear plot; (b) log–log plot of $F_1/(6\pi\mu a U_1)$ against the non-dimensional gap-width ϵ for the case of a force imposed on a sphere above a plane, with the force acting normal to the plane. ——, FCM simulation with only the force-monopole term included; ----, FCM simulation with both force-monopole and -dipole terms; ○, exact data from Brenner [4]; ×, exact data from [23]; ▷, exact data from [8].

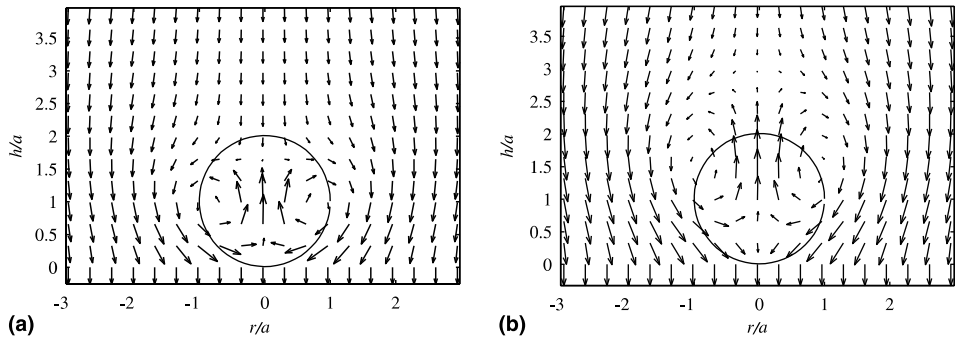

Fig. 4. Vector field plots for the case of a sphere sedimenting towards a wall, for a frame in which the sphere is at rest. h is the distance from the wall and r is the distance, measured parallel to the wall, from the particle center. (a) Simulation using both force-monopole and force-dipole terms; (b) simulation using only the force-monopole terms.

actual sphere, whereas, in the case where we only use the force-monopole term the virtual sphere is larger than the actual sphere.

Imposed force parallel to the wall. We impose a force on the sphere, parallel to the wall. For concreteness, suppose the force is in the $\mathbf{e}_2$-direction. The sphere translates parallel to the direction of the force, and it also rotates about a diameter parallel to $\mathbf{e}_3$. Thus the flow is a like that illustrated in Fig. 2, with $U_1 = 0$ and U_2, Ω_3 non-zero. Since there is no external torque on the sphere, Eq. (11) implies that

$$\frac{a\Omega_3}{U_2} = -\frac{\mathscr{C}_{32}}{\mathscr{D}_{33}}. \tag{13}$$

Thus Eq. (10) yields

$$\frac{F_2}{6\pi\mu a U_2} = -\frac{\mathscr{A}_{22}\mathscr{D}_{33} - \mathscr{B}_{23}\mathscr{C}_{32}}{\mathscr{D}_{33}}. \tag{14}$$

From Table 1 we see that the leading order term here is $O(\log\epsilon)$. In Fig. 5 we compare the ratio $F_2/(6\pi\mu a U_2)$. Again the FCM performs well away from the wall, but its accuracy decreases as $\epsilon \to 0$. When $\epsilon = 0$, in the case of the FCM simulations, the ratio $F_2/(6\pi\mu a U_2)$ takes on finite values, namely 1.93 and 2.22 for the simulation using the force-monopole term alone and that which includes the force-dipole

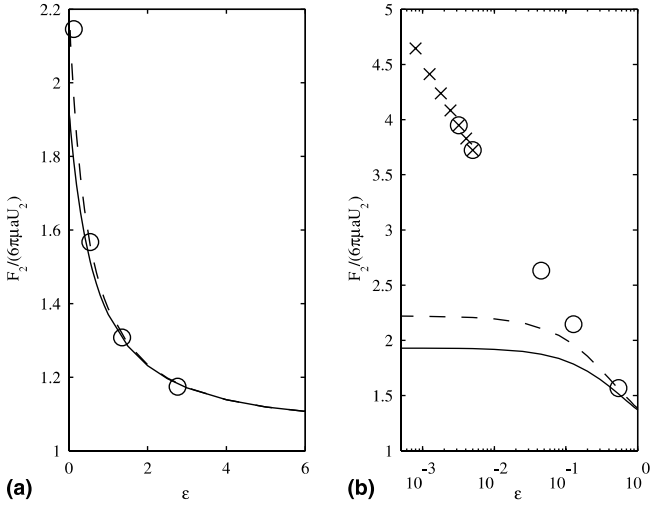

Fig. 5. (a) Linear plot; (b) log–linear plot of $F_2/(6\pi\mu a U_2)$ against the non-dimensional gap-width ϵ for the case of a force imposed on a sphere near a plane, with the force acting parallel to the plane. ——, FCM simulation with only the force-monopole term included; ----, FCM simulation with both force-monopole and -dipole terms; ○, exact data from [17]; ×, exact data from [7,39].

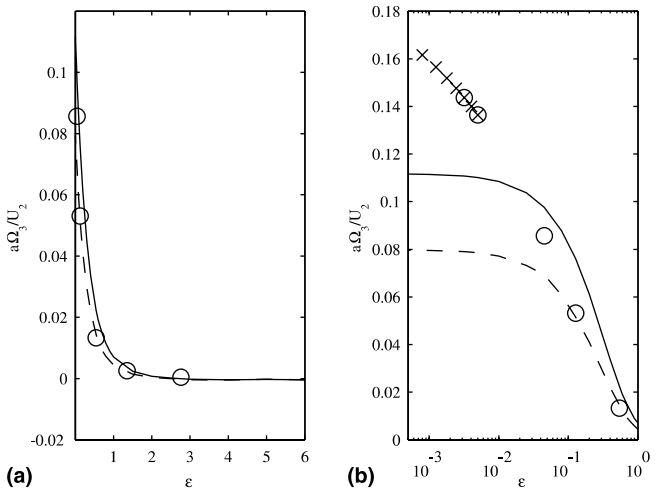

Fig. 6. (a) Linear plot; (b) log–linear plot of $a\Omega_3/U_2$ against the non-dimensional gap-width ϵ for the case of a force imposed on a sphere near a plane, with the force acting parallel to the plane. ——, FCM simulation with only the force-monopole term included; ----, FCM simulation with both force-monopole and -dipole terms; ○, exact data from [17]; ×, exact data from [7,39].

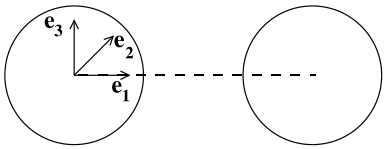

Fig. 7. Illustration of the particle–particle based axes. One axis is parallel to the line joining the centers of the particles. The other axes are taken to be orthogonal to both the line of centers and each other. The axes form a right-handed set.

correction, respectively. The data has been fitted to quadratic polynomials, given in Appendix D. In Fig. 6 we compare the ratio $a\Omega_3/U_2$ for the FCM simulations and for the exact data. For the FCM simulations, the ratio takes on finite values when $\epsilon = 0$, namely 0.111 and 0.0798 for the simulation using the force-monopole term alone and that which includes the force-dipole, respectively. Whilst the exact solution is singular, it only exhibits $O(\log \epsilon)$ singularities, thus the magnitude of the error in the FCM simulations is much smaller than in the previously discussed squeezing flow, where the singularity is $O(\epsilon^{-1})$. The effect of the force-dipole term is also much less pronounced than in the previous case.

3.2. Particle–particle interactions

The resistance problem for a pair of isolated identical spheres, α and β, may be written

$$F_i^\alpha = 6\pi\mu a\Big(\mathscr{A}_{ij}^\alpha U_j^\alpha + \mathscr{A}_{ij}^\beta U_j^\beta + a\mathscr{B}_{ij}^\alpha \Omega_j^\alpha - a\mathscr{B}_{ij}^\beta \Omega_j^\beta\Big), \tag{15}$$

$$F_i^\beta = 6\pi\mu a\Big(\mathscr{A}_{ij}^\alpha U_j^\beta + \mathscr{A}_{ij}^\beta U_j^\alpha + a\mathscr{B}_{ij}^\beta \Omega_j^\alpha - a\mathscr{B}_{ij}^\alpha \Omega_j^\beta\Big), \tag{16}$$

$$T_i^\alpha = 8\pi\mu a^2\Big(\mathscr{C}_{ij}^\alpha U_j^\alpha + \mathscr{C}_{ij}^\beta U_j^\beta + a\mathscr{D}_{ij}^\alpha \Omega_j^\alpha - a\mathscr{D}_{ij}^\beta \Omega_j^\beta\Big), \tag{17}$$

$$T_i^\beta = 8\pi\mu a^2\Big(-\mathscr{C}_{ij}^\beta U_j^\alpha - \mathscr{C}_{ij}^\alpha U_j^\beta - a\mathscr{D}_{ij}^\beta \Omega_j^\alpha + a\mathscr{D}_{ij}^\alpha \Omega_j^\beta\Big). \tag{18}$$

Table 2
Lubrication theory results and O(1) corrections for a pair of isolated identical spheres

		Inner solution		O(1)			References
$\mathscr{A}_{11}^\alpha$	=	$-\frac{1}{4}\epsilon^{-1} + \frac{9}{40}\log\epsilon + \frac{3}{112}\epsilon\log\epsilon$	+	−0.995	+	$O(\epsilon)$	[2,8,23,24,29,45]
$\mathscr{A}_{11}^\beta$	=	$\frac{1}{4}\epsilon^{-1} - \frac{9}{40}\log\epsilon - \frac{3}{112}\epsilon\log\epsilon$	+	0.350	+	$O(\epsilon)$	[2,8,23,24,29,45]
$\mathscr{A}_{22}^\alpha$	=	$\frac{1}{6}\log\epsilon$	+	−0.998	+	$O(\epsilon)$	[2,24,25,29,38]
$\mathscr{A}_{22}^\beta$	=	$-\frac{1}{6}\log\epsilon$	+	0.274	+	$O(\epsilon)$	[2,24,25,29,38]
$\mathscr{B}_{23}^\alpha$	=	$-\frac{1}{6}\log\epsilon - \frac{1}{12}\epsilon\log\epsilon$	+	−0.159	+	$O(\epsilon)$	[24,25,29,38]
$\mathscr{B}_{23}^\beta$	=	$\frac{1}{6}\log\epsilon + \frac{1}{12}\epsilon\log\epsilon$	+	0.001	+	$O(\epsilon)$	[24,25,29,38]
$\mathscr{D}_{11}^\alpha$	=	$\frac{1}{8}\epsilon\log\epsilon$	+	−1.052	+	$O(\epsilon)$	[24–26]
$\mathscr{D}_{11}^\beta$	=	$-\frac{1}{8}\epsilon\log\epsilon$	+	−0.150	+	$O(\epsilon)$	[24–26]
$\mathscr{D}_{33}^\alpha$	=	$\frac{1}{5}\log\epsilon + \frac{47}{250}\epsilon\log\epsilon$	+	−0.703	+	$O(\epsilon)$	[24,25,29,38]
$\mathscr{D}_{33}^\beta$	=	$-\frac{1}{20}\log\epsilon - \frac{31}{500}\epsilon\log\epsilon$	+	−0.027	+	$O(\epsilon)$	[24,25,29,38]

The complete set of resistance and mobility functions for an isolated pair of unequal particles is given in [24,29]. We tabulate the near-field forms here, since there are some typographic discrepancies in the literature. We refer to right-handed orthonormal axes with the $\mathbf{e}_1$ direction along the line of centers (i.e., the line joining the two particles), the other directions are chosen orthogonal to this, in order to form a set of right-handed axes (see Fig. 7). With respect to these axes, the tensors $\mathscr{A}^\gamma, \mathscr{B}^\gamma, \mathscr{C}^\gamma, \mathscr{D}^\gamma$ $(\gamma = \alpha, \beta)$ have the same symmetry properties as the particle–wall configuration. Table 2 gives the values of the non-zero entries. As in Table 1 we have standardized and cross-checked the results from the listed references. The O(1) terms are taken from [24].

The FCM results for pair configurations are given in [34]. They are qualitatively similar to the results for sphere–wall arrangements. We tabulate polynomial fits to the FCM data in Appendix D.

4. Implementing lubrication effects in the FCM

We have seen that the performance of the FCM degrades as particles come close to solid boundaries, be they other particles or container walls. We wish to develop a systematic method of correcting the velocities of affected particles: we do this by applying an additional force to each affected particle. We shall call these additional forces *barrier forces*. The particulars of the calculation are given below, but it is useful to have an intuitive idea of the method before tackling the details.

The FCM is set up as a mobility problem, i.e., given the forces on the particles and their positions, we may calculate their velocities. In the lubrication parameterization, we calculate new input forces based on the exact theory for pairwise and particle–wall interactions. For example, in the pairwise calculations, we isolate a given pair and balance an adjusted FCM force input with the hydrodynamic drag due to lubrication theory. This allows us to calculate the theoretical velocity for each of a pair of spheres in the corresponding configuration for an unbounded domain. We are then able to compute the required force input to the FCM to reproduce these velocities. Summing over all interactions gives us the barrier on each particle. Thus, in the lubrication parameterization, the barrier forces on the particles are not singular, but particle velocities go to zero as the gap-width decreases.

We will find it useful to introduce some notation. For each particle i we define a set $C_i(R)$ of all other particles closer than a a given distance R from i, i.e., $C_i(R) = \{j : \|\mathbf{Y}^{(i)} - \mathbf{Y}^{(j)}\| < R\}$. We also define a set $W(R)$ consisting of all particles closer than a distance R to the wall, i.e., $W(R) = \{i : |\mathbf{Y}^{(i)} \cdot \hat{\mathbf{n}}| < R\}$ where $\hat{\mathbf{n}}$ is the unit normal to the plane of the wall. An example is illustrated in Fig. 8.

Suppose we fix a cut-off length-scale $R = R_\mathrm{p}$ such that we wish to correct interactions for each particle pair with an interparticle distance less than R_p, and an $R = R_\mathrm{w}$ such that we wish to correct the velocities of particles closer than a distance R_w from the wall, then the total force-monopole term for particle i will be

$$\mathscr{F}^{(i)} = \mathbf{F}^{(i)} + \sum_{j \in C_i(R_\mathrm{p})} \mathbf{B}^{(ij)} + I_{W(R_\mathrm{w})}(i)\mathbf{B}^{(iw)}, \tag{19}$$

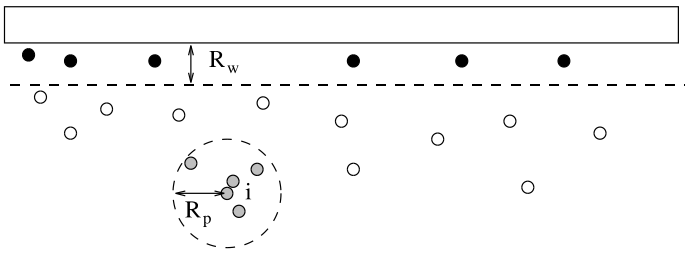

Fig. 8. Example of the sets $W(R_\mathrm{w})$ and $C_i(R_\mathrm{p})$. The black particles are in the set $W(R_\mathrm{w})$. The patterned particles are in the set $C_i(R_\mathrm{p})$.

where $\mathbf{F}^{(i)}$ is the body force on the particle (e.g., its weight), $\mathbf{B}^{(ij)}$ is the lubrication barrier force calculated for the pairwise interaction $i-j$ and $\mathbf{B}^{(iw)}$ is the lubrication barrier force for the interaction between particle i and the wall. $I_{W(R_w)}$ is the characteristic function for the set $W(R_w)$, which ensures that the particle-i–wall barrier force is added on only when particle i is sufficiently close to the wall.

The barrier calculation proceeds as follows: at the nth time level

Step 1. Solve the Stokes equations using only the applied external force-monopole, $\mathbf{F}^{(i)}$. It is not necessary at this stage to do the dipole iteration.

Step 2. Compute all the particle velocities, $\mathbf{U}_*^{(i)}(t_n)$.

Step 3. Find all the particles close to the wall and all close pairs of particles. In other words, compute the sets $C_i(R_p)$ for each i and $W(R_w)$ for each wall.

Step 4. Calculate the lubrication barrier forces:

- The wall interactions: for each particle i in $W(R_w)$ compute $\mathbf{B}^{iw}$.
- The pairwise interactions: for every particle i compute $\mathbf{B}^{ij}$ for each $j \in C_i(R_p)$.

See below for details of the calculations. Note that each interaction is considered independently and no iteration is required.

Step 5. Sum the barrier forces using Eq. (19).

Step 6. Solve the full flow equations, using the full force-monopole term and including the force-dipole.

Step 7. Calculate new particle velocities, $\mathbf{U}^{(i)}(t_n)$.

Step 8. Advect the particles with their new velocities and advance time.

4.1. Calculating particle–wall barrier forces

If a single particle is close to a wall, we saw in Section 3.1 that using the FCM, the ratio $F_k/(6\pi\mu a U_k)$ depends only on the direction of the force relative to the wall, the non-dimensional distance ϵ between the sphere surface and the plane-wall and the number of FCM-multipole terms used in the simulation. Taking the same axes as in Section 3.1, we write

$$\gamma_k^{\mathrm{FCM}}(\epsilon) = \frac{F_k}{6\pi\mu a U_k}. \tag{20}$$

The functions γ_k^{FCM} can be determined empirically, and are given in Appendix D. The component orthogonal to the wall corresponds to $k=1$ and a squeezing flow. The components parallel to the wall correspond to $k=2,3$ and shearing flows.

In the general case, suppose particle i is close to the wall at the nth time level (i.e., $i \in W(R_w)$). It is affected by all the other particles in the flow, and Eq. (20) does not hold exactly. We introduce an additional unknown hydrodynamic force $H_k^{(i)}(t_n)$ to account for the effects of the other particles, wall effects from the other side of the channel, etc., which is calculated from

$$\frac{F_k^{(i)} + H_k^{(i)}(t_n)}{6\pi\mu a U_*^{(i)}(t_n)} = \gamma_k^{\text{FCM-M}}(\epsilon), \tag{21}$$

where $\gamma_k^{\text{FCM-M}}$ is the appropriate functional form for calculations without force-dipole terms.

The force on the particle balances the drag:

$$F_k^{(i)} + H_k^{(i)} = -6\pi\mu a U_k^{(i),\mathrm{lub}} \lambda_k(\epsilon), \tag{22}$$

where λ_k is set using the exact resistance tensors of Table 1 as

$$\lambda_1 = \mathscr{A}_{11},$$

$$\lambda_2 = \frac{\mathscr{A}_{22}\mathscr{D}_{33} - \mathscr{B}_{23}\mathscr{C}_{32}}{\mathscr{D}_{33}},$$

$$\lambda_3 = \frac{\mathscr{A}_{33}\mathscr{D}_{22} - \mathscr{B}_{32}\mathscr{C}_{23}}{\mathscr{D}_{22}}.$$

This enables us to calculate a value for the lubrication velocity, $U_k^{(i),\mathrm{lub}}$. Then we set

$$\frac{F_k^{(i)} + B_k^{(iw)} + H_k^{(i)}(t_n)}{6\pi\mu a \gamma_k^{\text{FCM-MD}}(\epsilon)} = U_k^{(i),\mathrm{lub}}. \tag{23}$$

At this stage, we use the form of γ_k^{FCM} which applies to simulations which include both monopole and dipole multipole terms. We solve Eq. (23) for the wall lubrication barrier $B_k^{(iw)}$.

4.2. Calculating particle–particle barrier forces

At the nth time level, suppose we have found a particle pair (i, j) such that $j \in C_i(R_\mathrm{p})$, i.e., the particles are closer together than our cut-off lengthscale R_p. We calculate a set of three direction vectors, along which we will take components of the force and velocity. These correspond to the axes in Section 3.2. In the following all forces and velocities are assumed to be the components parallel to one of these directions.

We shall need the following result in our calculations: suppose that particle i and particle j are the only particles in an unbounded domain of quiescent fluid. A useful property of the FCM model is that

$$\frac{F_k^{(i)} - F_k^{(j)}}{6\pi\mu a(U_k^{(i)} - U_k^{(j)})} = \gamma^{\mathrm{FCM}}(\epsilon, \phi), \tag{24}$$

where γ depends on ϵ, the non-dimensional gap-width, ϕ, the angle between the line of centers and that of the $\hat{\mathbf{e}}_k$ direction and the number of FCM-multipole terms included in the simulation. The proof follows from the definition of the FCM Oseen tensor (see [37]). γ is determined empirically and given in Appendix D.

We use a modified version of Eq. (24) in which we introduce unknowns $\mathbf{H}^{(i)}$ and $\mathbf{H}^{(j)}$ to take into account the hydrodynamic effects of the container walls and other particles in the flow. Thus

$$\frac{\left(F_k^{(i)} + H_k^{(i)}(t_n)\right) - \left(F_k^{(j)} + H_k^{(j)}(t_n)\right)}{6\pi\mu a\left(U_*^{(i)}(t_n) - U_*^{(j)}(t_n)\right)} = \gamma_k^{\text{FCM-M}}(\epsilon). \tag{25}$$

Here, we take $\gamma_k^{\text{FCM-M}}$ to be the correct functional form for the component being calculated (squeezing flow or shearing flow) and for the form of the FCM without dipole terms. Thus the only unknowns in Eq. (25) are $H_k^{(i)}(t_n)$ and $H_k^{(j)}(t_n)$.

Next we impose a condition that the pairwise lubrication drag forces on each particle are equal and opposite, and may be balanced by the force on each particle:

$$\text{drag on particle } i = -(\text{drag on particle } j) \tag{26}$$

$$F_k^{(i)} + H_k^{(i)} = -(\text{drag on particle } i)_k, \tag{27}$$

$$F_k^{(j)} + H_k^{(j)} = -(\text{drag on particle } j)_k, \tag{28}$$

$$\Rightarrow\ H_k^{(i)} + H_k^{(j)} = -(F_k^{(i)} + F_k^{(j)}). \tag{29}$$

Eqs. (29) and (25) form a closed system for $H_k^{(i)}$ and $H_k^{(j)}$. We may now revisit the particle pair resistance problem, (Eqs. (15)–(18)) and observe that

$$\begin{aligned}(\text{drag on particle } i)_k - (\text{drag on particle } j)_k &= (F_k^{(i)} + H_k^{(i)}) - (F_k^{(j)} + H_k^{(j)}) \\ &= -6\pi\mu a\lambda_k(U_k^{(i),\text{lub}} - U_k^{(j),\text{lub}}),\end{aligned}$$

where λ_k is set using the exact resistance tensors of Table 2 as

$$\lambda_1 = \mathscr{A}_{11}^{\alpha} - \mathscr{A}_{11}^{\beta},$$

$$\lambda_2 = \frac{(\mathscr{A}_{22}^{\alpha} - \mathscr{A}_{22}^{\beta})(\mathscr{D}_{33}^{\alpha} - \mathscr{D}_{33}^{\beta}) - (\mathscr{B}_{23}^{\alpha} - \mathscr{B}_{23}^{\beta})(\mathscr{C}_{32}^{\alpha} - \mathscr{C}_{32}^{\beta})}{\mathscr{D}_{33}^{\alpha} - \mathscr{D}_{33}^{\beta}},$$

$$\lambda_3 = \frac{(\mathscr{A}_{33}^{\alpha} - \mathscr{A}_{33}^{\beta})(\mathscr{D}_{22}^{\alpha} - \mathscr{D}_{22}^{\beta}) - (\mathscr{B}_{32}^{\alpha} - \mathscr{B}_{32}^{\beta})(\mathscr{C}_{23}^{\alpha} - \mathscr{C}_{23}^{\beta})}{\mathscr{D}_{22}^{\alpha} - \mathscr{D}_{22}^{\beta}},$$

since there is no net torque on either particle. This gives us the value of the velocity of particle i, relative to particle j. By analogy with Eq. (25) we set

$$\frac{\left(F_k^{(i)} + B_k^{(ij)}(t_n) + H_k^{(i)}(t_n)\right) - \left(F_k^{(j)} + B_k^{(ji)}(t_n) + H_k^{(j)}(t_n)\right)}{6\pi\mu a\gamma_k^{\text{FCM-MD}}(\epsilon)} = U_k^{(i),\text{lub}} - U_k^{(j),\text{lub}}, \tag{30}$$

which, upon rearrangement, gives one expression for the difference between the lubrication barrier forces $B_k^{(ij)}(t_n) - B_k^{(ji)}(t_n)$ at the nth time level. (Note that we use the form of γ_k^{FCM} for calculations using both monopole and dipole multipoles at this stage.) To close the system we use another condition:

$$B_k^{(ij)}(t_n) + B_k^{(ji)}(t_n) = 0, \tag{31}$$

so that there is no resultant force on the center of mass of the particle pair.

Note that the barrier force calculation is carried out independently for each pair, with no iteration. The effect of iterating the scheme is considered in Section 5.2.

5. Example simulations

In tests, the lubrication parameterization recovers the exact results for isolated particle pairs and individual particles near a single wall. In this section we consider how it fares in different geometries.

5.1. Particle in a channel

Lomholt and Maxey [34] compared FCM simulations to exact results from [13,14] for a particle in a channel. They found that at small distances between the particle and the channel wall the FCM did not agree with the exact results. In this section we compare lubrication parameterization simulations for small particle–wall distances. Fig. 9 describes the geometry of the flows. A sphere of radius a is placed in a channel with a height H. The dimensional parameter α, controls the center-line velocity of the parabolic Poiseuille velocity profile. F_1 and F_2 are the imposed forces on the sphere, perpendicular and parallel to the channel walls, respectively. b is the distance of the sphere center from the bottom wall of the channel.

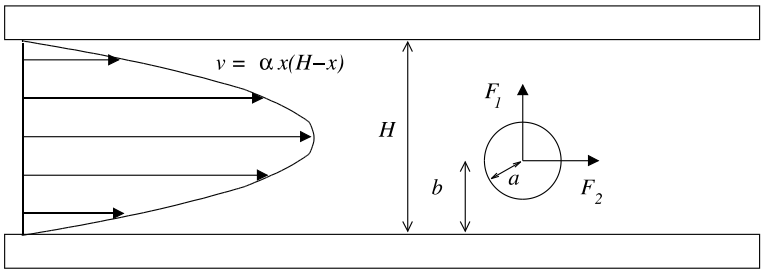

Fig. 9. Channel geometry.

The code used is described in Appendix C. The height of the channel in the wall-normal direction was set to be $H = 2$. We fixed the ratio of the height of the particle center above the bottom wall to the particle radius, $b/a = 1.1$, but varied the ratio of the particle center height to the channel height, $s = b/H$. The particle radius a was varied accordingly. Thus, the particle is always close to the bottom wall, but the relative influence of the top wall is governed by s.

The length of the channel in the periodic directions was set at $30a$, and thus varied with the particle radius. The resolution in these periodic directions was chosen so that there were at least 6 points inside the particle in each direction. The distance R_w, the distance between the particle center and the wall at which the lubrication barrier is switched on, was $1.25a$. Thus the barrier along the bottom wall was active for all of the following simulations. The barrier along the top wall was only active when $s = 0.5$, corresponding to the situation where the sphere is in the center of the channel. The value of R_w only affects when the lubrication barrier is activated: it is not involved in the calculation of the barrier forces as a parameter.

5.1.1. Imposed force perpendicular to the walls

The geometry for the motion is given by Fig. 9 with $\alpha = 0$, $F_1 = 6\pi\mu a$ (the force required for an isolated particle to move with a velocity of 1.0) and $F_2 = 0$. Thus there is no flow in the channel, except for that due to a particle sedimenting towards the bottom wall. The resistance problem for this geometry is similar to that for the single wall–particle configurations of Section 3.1. We use the same notation for the resistance tensors. In Fig. 10 we plot the drag coefficient

$$-\mathscr{A}_{11} = \frac{F_1}{6\pi\mu a U_1}, \tag{32}$$

for various values of $s = b/H$. Recall that the ratio b/a is fixed at 1.1, so the sphere is always close to the bottom wall. The figure illustrates the improvement of the FCM when the lubrication parameterization is used. Note that since the parameterization is tuned for a sphere close to a single plane wall, the results are excellent for small s, when the relative effect of the upper wall is negligible. For intermediate s the effect of the upper wall has some importance, and there is an evident quantitative difference between the results for the lubrication parameterization and the exact results. Nevertheless, these results still show an improvement over the simple FCM model. For $s = 0.5$ the particle is located exactly in the center of the channel. Thus, the lubrication parameterization is employed for both walls additively. The lubrication barrier force from each wall acts to retard the particle motion; these forces do not cancel out. We see that the monopole-only version of the code is able to reproduce the exact results to within about 1% whereas the error for the simulations using both monopole and dipole is about 28%. The reason for this discrepancy is that in the center of the channel, the geometry is symmetric, so the rate of strain on the particle is zero. Thus, the dipole term is zero, but the function $\gamma_k^{\text{FCM-MD}}$ employed in the the lubrication parameterization is still that

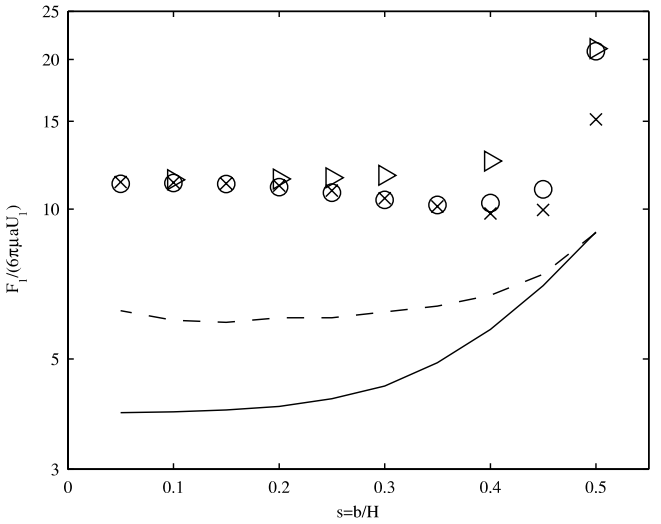

Fig. 10. Particle in a channel, sedimenting perpendicular to the channel walls. Semilog plot of the drag coefficient $F_1/(6\pi\mu a U_1)$ versus $s = b/H$. ——, FCM simulation with only the force-monopole term from [34]; ----, FCM simulation with both force-monopole and -dipole terms from [34]; ○, FCM simulation using the lubrication parameterization with only one force term; ×, FCM simulation using the lubrication parameterization with both force terms (monopole and dipole); ▷, exact data from [13].

for a simulation using the dipole term. This function is for a single wall geometry. At this distance from a single wall, the dipole would have a significant retarding effect on the particle. Thus using $\gamma_k^{\text{FCM-MD}}$ in Eq. (23) we underestimate the required lubrication barrier forces. Situations involving intermediate s or such that the rate of strain on the particle is zero are unlikely to occur in dealing with a reasonably sized random suspension. In the case that the flow required was in a geometry with nearby walls such as a narrow channel, the problems could be fixed by using a γ_k^{FCM} function calculated from the pure FCM results for flow in such a channel.

5.1.2. Imposed force parallel to the walls

The geometry for the motion is given by Fig. 9 with $\alpha = 0$, $F_1 = 0$ and $F_2 = 6\pi\mu a$. Thus the only flow is that caused by an imposed force on the particle, parallel to the walls. In Fig. 11 we plot the velocity ratios

$$\frac{a\Omega_3}{U_2} = -\frac{\mathscr{C}_{32}}{\mathscr{D}_{33}} \tag{33}$$

and the drag coefficient

$$\frac{F_2}{6\pi\mu a U_2} = -\frac{\mathscr{A}_{22}\mathscr{D}_{33} - \mathscr{B}_{23}\mathscr{C}_{32}}{\mathscr{D}_{33}} \tag{34}$$

for various values of $s = b/H$. We see that the ratio $a\Omega_3/U_2$ (panel (a)) is preserved when the simple FCM is augmented by the lubrication parameterization. This is due to the linearity of the governing equations: the lubrication barrier modifies the value of the force-monopole term only. For a given distance from the wall, the particle velocity, angular velocity and force-dipole terms are all proportional to the value of the force-monopole.

For the drag coefficient, $F_2/(6\pi\mu a U_2)$ we see a marked improvement in using the lubrication parameterization over the simple FCM. The change in the error with s is less marked than in the previous case, which is an indication that upper wall has less influence in this type of flow.

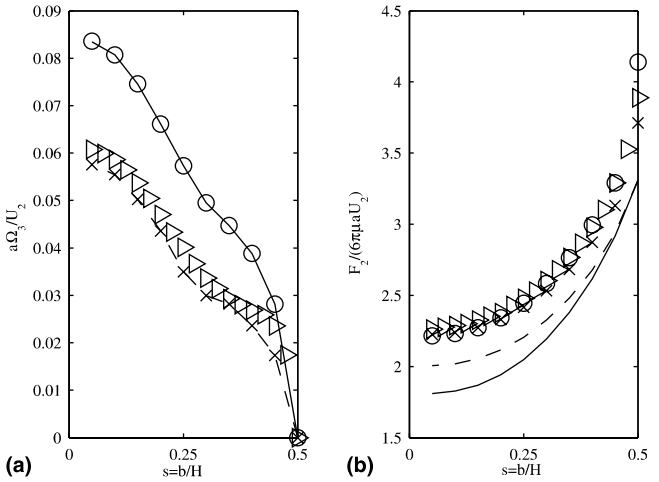

Fig. 11. Particle in a channel, with an imposed force parallel to the channel walls. (a) Plot of the ratio $a\Omega_3/U_2$ versus $s = b/H$; (b) plot of the ratio $F_2/(6\pi\mu a U_2)$ versus s. ——, FCM simulation with only the force-monopole term included; ----, FCM simulation with both force-monopole and -dipole terms; ○, FCM simulation using the lubrication parameterization with only one multipole term; ×, FCM simulation using the lubrication parameterization with both multipole terms (monopole and dipole); ▷, exact data from [14].

5.1.3. Neutrally buoyant sphere in Poiseuille flow

The geometry for the motion is given by Fig. 9 with $H^2\alpha = 1$, so that the center-line velocity $V_c = 0.25$. The sphere is neutrally buoyant, so we set $F_1 = 0$ and $F_2 = 0$. The particle is present through the use of the force-dipole term alone.

Since the fluid is not at rest at infinity, the resistance problem must be augmented

$$F_i = 6\pi\mu a\left(\mathscr{A}_{ij}U_j + a\mathscr{B}_{ij}\Omega_j + \mathscr{K}_{ij}V_j^c\right), \tag{35}$$

$$T_i = 8\pi\mu a^2\left(\mathscr{C}_{ij}U_j + a\mathscr{D}_{ij}\Omega_j + \mathscr{L}_{ij}V_j^c\right). \tag{36}$$

In this particular case, with $\mathbf{V}^c = V_c\mathbf{e}_2$, the only relevant non-zero components of $\mathscr{K}$ and $\mathscr{L}$ are $\mathscr{K}_{22}$ and $\mathscr{L}_{32}$. The sphere is neutrally buoyant, so we may set the left-hand-side of Eqs. (35) and (36) equal to zero. Thus we find the following ratios:

$$\frac{U_2}{V_c} = -\frac{\mathscr{K}_{22}\mathscr{D}_{33} - \mathscr{L}_{32}\mathscr{B}_{23}}{\mathscr{A}_{22}\mathscr{D}_{33} - \mathscr{C}_{32}\mathscr{B}_{23}}, \tag{37}$$

$$\frac{a\Omega}{V_c} = \frac{\mathscr{K}_{22}\mathscr{C}_{32} - \mathscr{L}_{32}\mathscr{A}_{22}}{\mathscr{A}_{22}\mathscr{D}_{33} - \mathscr{C}_{32}\mathscr{B}_{23}} \tag{38}$$

which are plotted in Fig. 12. These results indicate that the lubrication model offers an improvement over the simple FCM for a case involving a background flow. Again we see an increase in error as s increases. It should be noted that the simple FCM is able to give very good results for the tensors $\mathscr{K}$ and $\mathscr{L}$ [34]. The discrepancy between the simple FCM and the exact results is caused by errors in the other tensors, $\mathscr{A}, \mathscr{B}, \mathscr{C}, \mathscr{D}$ as was illustrated in the previous sections.

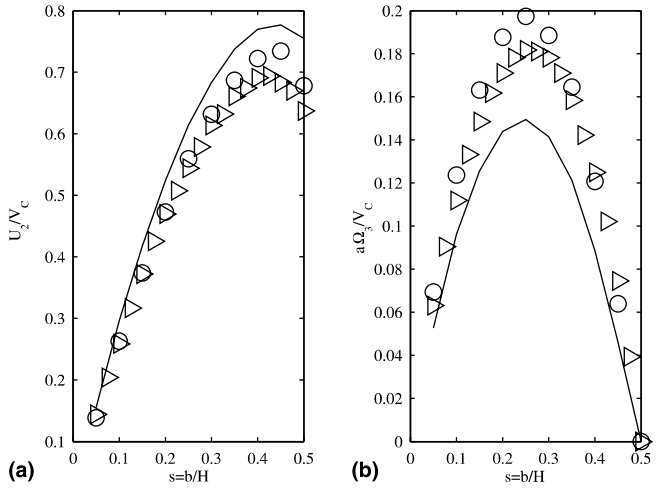

Fig. 12. Neutrally buoyant sphere in a Poiseuille flow. (a) Plot of the ratio U_2/V_c versus $s = b/H$; (b) plot of the ratio $a\Omega_3/V_c$ versus s. —, FCM simulation with both force-monopole and -dipole terms from [34]; ○, FCM simulation using the lubrication parameterization with both force terms (monopole and dipole); ▷, exact data from [14].

5.2. Horizontal seven sphere chain

The results in this section were computed using the analytic expression for the FCM-Oseen tensor, given in [37]. We calculate local values of the flow field by accurate numerical integration using weighted sums.

A horizontal chain of spheres, illustrated in Fig. 13, with a center to center spacing of 2.005 radii is modeled and the results compared to those computed by Ganatos et al. [12]. The spheres sediment under gravity, with the middle sphere moving fastest. Fig. 14 shows instantaneous results for the drag correction factor, $F/(6\pi\mu aU)$ and the sphere angular velocities. The results are given for only half the chain due to symmetry. Ganatos et al. estimate their maximum probable error to be 0.4% for the drag correction factor and 5% for the angular velocities. An additional uncertainty is introduced through the measurement of data from their plots. We estimate the maximum of this error to be approximately 2% in the case of the drag coefficients and as much as 10% for the angular velocities. The performance of the lubrication parameterization improves upon that of the simple FCM for the inner spheres, but degrades for the outer spheres in the chain. This is illustrative of the limitations of applying the lubrication barrier in a pairwise fashion. In this case we see that the lubrication barrier on particle 2 is affected by its interaction with both particles 1 and 3, whereas the lubrication barrier on particle 3 is only calculated from its interaction with particle 2, even though it is indirectly affected by particle 1. This results in the outermost sphere having a velocity which is too high. Iterating the lubrication barrier calculation would not lead to improvement. After one pass through the lubrication parameterization scheme, the relative velocity between particles 2 and 3 is still higher than that which would be expected for an isolated pair. A second pass through the scheme would act to reduce this relative velocity, resulting in an additional force in the downward direction on the outermost sphere, exacerbating the problem.

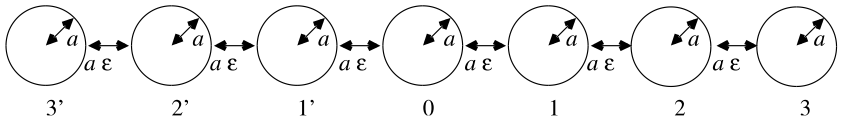

Fig. 13. Illustration of seven sphere horizontal chain. Note that the central sphere is numbered zero. The chain is symmetric about this sphere.

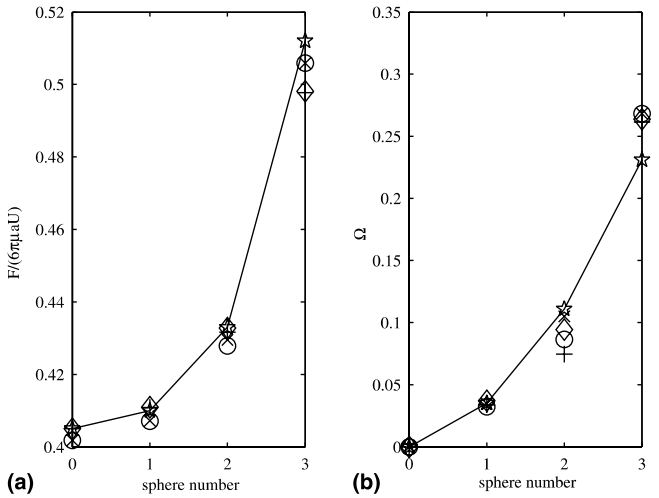

Fig. 14. Seven sphere chain sedimenting perpendicular to its line of centers. (a) Plot of the ratio $F/(6\pi\mu aU)$; (b) plot of the angular velocity Ω. ○, FCM with only one force term; ×, FCM with both force-monopole and -dipole terms; +, FCM with the force-monopole term and lubrication parameterization; ◇, FCM with both force terms and the lubrication parameterization; ☆, results from [12]. Note that due to symmetry we only need give results for half the chain.

5.3. Homogeneous random suspension with periodic boundary conditions

We model a homogeneous random suspension in a periodic domain, with a Fourier-pseudospectral code. The use of this code is documented in [37]. The domain size is taken to be $2\pi \times 2\pi \times 2\pi$, and we use a resolution of 128 points in each direction. We initially seed the flow with 1600 particles, distributed randomly in space. Each particle has radius 0.1305, corresponding to a total volume fraction of 6%. We neglect particle inertia in the calculations.

The code was run with the force-monopole term only. Each particle was subjected to a force of $6\pi\mu a$, which corresponds to the drag on an isolated particle with a Stokes settling velocity of 1. In this periodic domain, a single particle settling under the action of such a force settles with a velocity $V_0 = 0.941$.

The lubrication parameterization was employed with a variety of cut-off parameters, R_p. In addition, we used the repulsive potential force barrier (described in Appendix B). This acted only in the event that a pair of particles overlapped: the lubrication barrier is undefined for overlapping particles. The parameters used in the potential force barrier were $F_{ref} = 0.25 \times 6\pi\mu a$ and $R_{ref} = R_p$. On average, less than 3 particle pairs overlapped by more than 5% of a radius in a given time-step.

For each set of parameters, the system was run to a statistically stationary state, the initial results were discarded and the subsequent results time-averaged over a period of more than 2400 Stokes settling times ($t_S = a/V_0$). In Table 3 we give the mean particle settling velocity and mean square fluctuations for each

Table 3
Mean particle velocities and fluctuations

$R_p/2a$	$\langle V_\parallel \rangle / V_0$	$\langle (V'_\parallel)^2 \rangle / V_0^2$	$\langle (V'_\perp)^2 \rangle / V_0^2$	$\bar{n}$
1.05	0.7628 ± 0.0005	0.5552	0.0755	1.2634
1.10	0.7922 ± 0.0005	0.6832	0.0788	1.3221
1.20	0.7965 ± 0.0005	0.6684	0.0811	1.3473
1.30	0.8053 ± 0.0005	0.7281	0.0845	1.3605

value of R_p. The uncertainty in the mean settling velocity is calculated as the standard deviation of the mean. Also given is $\bar{n}$, the average number of particles neighboring each particle in the suspension. We consider two particles to be neighbors if their center–center interparticle distance is less than a cut-off length R_c. The value of $\bar{n}$ is an increasing function of R_c and is identically zero when R_c is less than the minimum particle separation distance in the suspension. In this case we take $R_c = 1.46 \times 2a$, since it is a convenient value above the largest R_p we considered. The results are not highly sensitive to the value of R_c chosen.

As we change R_p, the lubrication barrier cut-off parameter, we find that the variation in the mean particle settling velocity and fluctuations is not large. However, the dependence on R_p is systematic. The increase in the mean settling velocity with R_p may be explained by the fact that there is also more clustering of particles, as indicated by the values of $\bar{n}$. The lubrication drag forces act to reduce the relative velocity between particle pairs predicted by the FCM. Thus, particles remain closer together for longer, giving rise to greater clustering. As the lubrication cut-off parameter R_p increases, particles experience this sticking effect more of the time.

6. Conclusions

Previous work [34,37] has shown that the FCM smoothes out the flow close to the particle surface. At a distance of approximately $0.25 - 0.5a$ away from the surface, it reproduces the exact results. Consequently, the FCM performs well when distances between solid boundaries are sufficiently large, however it does not capture strong lubrication forces that act between particles in relative motion at small separations. The version of the model using two multipole terms, performs considerably better than the version with the monopole alone, since the dipole term enforces a constraint on the particle deformation.

We have developed a lubrication parameterization to improve the particle velocities for close interactions calculated using the FCM. This is achieved by considering individual interactions between particles and walls, and pairwise interparticle interactions. Lubrication barrier forces are calculated based upon our knowledge of exact results for isolated pairs of particles and particles interacting with a single wall. We also use our experience of the FCM in the corresponding situations. These forces are added onto the force-monopole term for each particle.

The lubrication parameterization reproduces the exact results for the particle velocities of an isolated pair of spheres and for a sphere near a single plane wall, which the modeling is tuned to. In general the lubrication parameterization improves the estimates of particle velocities, but not the form of the local flow field. However, having the correct local velocity will improve the flow in the far field. We tested the model to evaluate its performance in several additional geometries. The results indicated that where it is possible to isolate the effects of a particle and a single wall or a pairwise interaction, the lubrication parameterization performs well. With chains of close particles, or with a narrow channel this parameterization becomes less reliable. This is quantified in the results presented.

We also tested the case of a homogeneous random suspension with 1600 particles sedimenting in a periodic box. In addition to the lubrication parameterization we found it necessary to employ a repulsive force which acted only in the occasional event of particle overlap. We saw that the use of different cut-off lengthscales for the lubrication parameterization made some difference to the microstructure of the suspension and to the velocity of the bulk flow.

The use of the lubrication barrier is more computationally expensive than the use of a simple collision barrier, such as the potential force barrier of Eq. (B.1). For the case of potential force barrier simulations, at each time-step we must first determine neighboring pairs of particles. Checking each pair of particles in the domain would require $O(N^2)$ operations, where N is the number of particles. However, we may use a more efficient cell-index technique such as that described in [1]. This is an $O(NN_c)$ calculation, where N_c is the number of cells in the domain. Second, we must compute the potential force barrier for each pair of

neighbors. The number of operations involved scales linearly with the number of close particle pairs, N_p. Once the barriers have been calculated we must solve the forced Stokes equations, (1) and (2), for the flow field. The number of operations required in this calculation depends on the domain size and on the efficiency of the flow solver. Finally, we calculate the particle velocities ($O(N)$ operations) and advect the particles to new positions ($O(N)$ operations).

When using the lubrication barrier an additional computation of the flow field and particle velocities is required before calculating the lubrication barrier forces. Also, the computation of the lubrication barrier for each pair involves more operations, although this step still scales linearly with the number of close pairs, N_p. In practice, using the homogeneous random suspension code described in Section 5.3, we find that the computation time for simulations using the lubrication barrier is approximately twice that for simulations using the potential force barrier. We timed simulations using a serial code running on an IBM SP2, (one CPU of a 4-way PowerPC 604e (332 MHz) node), with a grid size of 128^3 and 1600 particles, corresponding to a volume fraction of 6%. The R_p parameter was set at $2.2a$. The wall clock time taken for initialization (identical for both barriers) plus 100 time-steps was 1765 s for the lubrication barrier run and 908 s for the potential force barrier simulation. Further investigation needs to be carried out before drawing a final conclusion as to whether the additional computational expense is justified by the inclusion of extra physics in the model.

Acknowledgements

This work was supported in part by DARPA-ATO and by a Simon Ostrach Graduate Fellowship. Computations were carried out at Brown University's Technology Center for Advanced Scientific Computing and Visualization and Boston University Scientific Computing Facilities. The authors would like to thank George Karniadakis and Sune Lomholt for their help.

Appendix A. Dipole iteration

For simulations of N particles, the exact computation of $S_{ij}^{(n)}$ involves the construction and solution of a $5N \times 5N$ linear system

$$\mathscr{L}\mathscr{S} = \mathscr{E},$$

where $\mathscr{L}$ represents the FCM Stokes flow operator which maps stresslet strengths to averaged particle strains. $\mathscr{L}$ is a linear operator which depends on the geometry of the system and the particle positions. $\mathscr{S}$ is the unknown, containing the independent components of the stresslet for each particle. $\mathscr{E}$ is the $5N$ vector containing all the independent elements of the strain for each particle, determined from the flow due to the external forces and torques on each particle.

In practice, we avoid building the coefficient matrix and compute the elements of $S_{ij}^{(n)}$ iteratively, exploiting our knowledge of the short range of the effect of the force-dipole on the flow. One such iterative scheme is described in [33]. Another, faster method is described below.

We use the following heuristic algorithm for the kth iteration step:

Step 1. Set $\mathscr{E} = \mathscr{E}^{k-1}$, the averaged rate of strain vector calculated from the flow due to the forces, torques and stresslets on each particle at the end of the $(k-1)$st iteration. If $\|\mathscr{E}\|_{\mathbb{R}^{5N}}$ is less than a given tolerance level terminate the iteration, otherwise continue.

Step 2. Set $\mathscr{S}^* = ((20\pi\mu a^3)/3)\mathscr{E}$ as a trial solution, since the stresslet for a single particle in a pure straining flow is $S_{ij} = ((20\pi\mu a^3)/3)E_{ij}$.

Step 3. Calculate the rate of strain in the flow due to $\mathscr{S}^*$ alone (do not include force-monopole or torque terms), i.e., $\mathscr{E}^* = \mathscr{L}\mathscr{S}^*$.

Step 4. Estimate a scale factor, $\lambda^{(n)}$ for each particle n. (This is explained below.)
Step 5. Set $S_{ij}^{(n),k} = S_{ij}^{(n),k-1} + \lambda^{(n)} S_{ij}^{(n),*}$ for each particle n.
Step 6. Calculate the flow due to the full monopole and dipole terms.
Step 7. $k := k + 1$.

Our choice for $\lambda^{(n)}$ is motivated as follows: suppose we have only one particle in the system, then $\mathscr{E} = (E_{11}, E_{12}, E_{13}, E_{22}, E_{23})^{\mathrm{T}}$, $\mathscr{S} = (S_{11}, S_{12}, S_{13}, S_{22}, S_{23})^{\mathrm{T}}$, etc. A simple calculation shows that

$$\min \|\mathscr{E} + \lambda \mathscr{E}^*\|$$

is achieved by setting $\lambda = -\mathscr{E}^* \cdot \mathscr{E} / \|\mathscr{E}^*\|$.

For multiple particles, we find that the dipole on one particle has a limited effect on the rate of strain on the others, unless they are close together. In this case we define vectors $\tilde{\mathscr{E}}$ and $\tilde{\mathscr{E}}^*$ for each particle. These contain those elements of $\mathscr{E}$ and $\mathscr{E}^*$ corresponding to the particle itself and its near neighbors. Near neighbors are defined as particles whose center–center distance is less than a a cut-off lengthscale. Typically this might be $O(2.5a)$. For example, if particles 1 and 2 are close, particles 2 and 3 are close but particle 4 is isolated from them all, then

$$\tilde{\mathscr{E}}^{(1)} = (E_{11}^{(1)}, \ldots E_{23}^{(1)}, E_{11}^{(2)}, \ldots E_{23}^{(2)})^{\mathrm{T}},$$

$$\tilde{\mathscr{E}}^{(2)} = (E_{11}^{(1)}, \ldots E_{23}^{(1)}, E_{11}^{(2)}, \ldots E_{23}^{(2)} E_{11}^{(3)}, \ldots E_{23}^{(3)})^{\mathrm{T}},$$

$$\tilde{\mathscr{E}}^{(3)} = (E_{11}^{(2)}, \ldots E_{23}^{(2)} E_{11}^{(3)}, \ldots E_{23}^{(3)})^{\mathrm{T}},$$

$$\tilde{\mathscr{E}}^{(4)} = (E_{11}^{(4)}, \ldots E_{23}^{(4)})^{\mathrm{T}}.$$

We define λ by

$$\lambda^{(n)} = \begin{cases} 0 & \text{if} \|\tilde{\mathscr{E}}^{(n)}\| < \text{tolerance}, \\ -\frac{\tilde{\mathscr{E}}^{(n),*} \cdot \tilde{\mathscr{E}}^{(n)}}{\|\tilde{\mathscr{E}}^{(n),*}\|} & \text{otherwise.} \end{cases}$$

For moderate volume fractions, the system converges after just a few iterations. For example, in a typical first time-step for a volume fraction of 11% the force-dipole converged after just 5 iterations (using the channel code of Appendix C, with dimensions of $10a$ in the wall-normal direction and $30a$ in the periodic dimensions, and 250 randomly seeded particles of radius $a = 1$ in the flow). The tolerance level used was $1\% \times V_s/a$, where V_s is the Stokes settling velocity of an isolated particle of the same size and weight. In contrast, for the same seeding of particles, the iteration method of Lomholt [33] failed to converge in 25 iterations. This iterative scheme also works well in finite *Re* flows [32].

Note that at the nth time-step, the dipole from the $(n-1)$st time-step is often a good approximation to the dipole at the current time. Thus, at later times in the simulation, the number of required iterations decreases.

Appendix B. Potential force collision barrier

The repulsive potential force collision barrier has been used by Climent and Maxey [6] to prevent unphysical particle overlaps in their simulations of homogeneous random suspensions.

For the case of a pair of particles, i and j, let $\mathbf{x}_{ij} = \mathbf{Y}^{(i)} - \mathbf{Y}^{(j)}$, and $r_{ij} = \|\mathbf{x}_{ij}\|$. If $r_{ij} < R_{\mathrm{ref}}$ then the barrier force

$$\mathbf{B}^{ij} = -\frac{F_{\text{ref}}}{2a}\left[\frac{R_{\text{ref}}^2 - r_{ij}^2}{R_{\text{ref}}^2 - 4a^2}\right]^2 \mathbf{x}_{ij} \tag{B.1}$$

is added to the force monopole on particle i. F_{ref} is a parameter with the dimensions of a force, usually taken to be a fraction of the buoyancy adjusted weight of the particle, and R_{ref} is a cut-off length. An analogous expression applies for the close approach of a particle to a wall. This two-parameter function was chosen for convenience, and its effects on the bulk flow are small, as long as the cut-off length R_{ref} is sufficiently short. A sensitivity analysis for the effects on the bulk flow for a range of parameters is given in [9]. Note that the force is antisymmetric in i, j: $\mathbf{B}^{ij} = -\mathbf{B}^{ji}$, and thus is consistent with Newton's third law.

Appendix C. Channel code

We wish to solve the Stokes equations

$$-\mu\nabla^2\mathbf{u} + \nabla p = \mathbf{f}, \tag{C.1}$$

$$-\nabla \cdot \mathbf{u} = 0 \tag{C.2}$$

for velocity, $\mathbf{u} = (u, v, w)$ and pressure, p, in a domain $(0, L_x) \times (0, L_y) \times (0, L_z)$ subject to homogeneous Dirichlet (no slip) conditions on the channel walls:

$$\mathbf{u}(0, y, z) = \mathbf{u}(L_x, y, z) = 0$$

and periodic boundary conditions in the y and z directions:

$$\mathbf{u}(x, 0, z) = \mathbf{u}(x, L_y, z) \quad \forall (x, z) \in (0, L_x) \times (0, L_z) \quad \text{and}$$

$$\mathbf{u}(x, y, 0) = \mathbf{u}(x, y, L_z) \quad \forall (x, y) \in (0, L_x) \times (0, L_y).$$

We use a mixed Fourier spectral element method to solve for the flow. A comprehensive introduction to spectral element methods as applied to computational fluid dynamics is given by Karniadakis and Sherwin [28].

Since the geometry is periodic in the wall-parallel directions, we may write the velocity, pressure and forcing in Fourier series representations:

$$\mathbf{u}(x, y, z) = \sum_{k,l} \hat{\mathbf{u}}(x, k, l) e^{i(\beta_y k y + \beta_z l z)},$$

$$p(x, y, z) = \sum_{k,l} \hat{p}(x, k, l) e^{i(\beta_y k y + \beta_z l z)},$$

$$\mathbf{f}(x, y, z) = \sum_{k,l} \hat{\mathbf{f}}(x, k, l) e^{i(\beta_y k y + \beta_z l z)},$$

where $\beta_y = 2\pi/L_y$ and $\beta_z = 2\pi/L_z$. For simplicity of notation, in the rest of this description we restrict to the case where $L_y = L_z$ and write $\beta = \beta_y = \beta_z$. The algorithm is easily generalized to the case of $L_y \neq L_z$, as indeed it is in the code.

In practice, this transformation is discretized by truncation of the Fourier series. The efficient fast Fourier transform (FFT) can be used to carry out the transformation between physical and spectral space.

The Fourier series transformation reduces the Stokes equations to a series of decoupled problems where we treat the wavenumbers as parameters:

$$-\mu\left(\frac{\mathrm{d}^2}{\mathrm{d}x^2}-\lambda^2\right)\hat{u}+\frac{\mathrm{d}\hat{p}}{\mathrm{d}x}=\hat{f}^{(1)},$$

$$-\mu\left(\frac{\mathrm{d}^2}{\mathrm{d}x^2}-\lambda^2\right)\hat{v}+\mathrm{i}\beta k\hat{p}=\hat{f}^{(2)},$$

$$-\mu\left(\frac{\mathrm{d}^2}{\mathrm{d}x^2}-\lambda^2\right)\hat{w}+\mathrm{i}\beta l\hat{p}=\hat{f}^{(3)},$$

$$-\left(\frac{\mathrm{d}\hat{u}}{\mathrm{d}x}+\mathrm{i}\beta k\hat{v}+\mathrm{i}\beta l\hat{w}\right)=0$$

with $\lambda^2=\beta^2(k^2+l^2)$.

The equivalent weak form is this: Find $(\hat{\mathbf{u}},\hat{p})$ in $X\times M$ such that

$$\mu\left\{\left(\frac{\mathrm{d}\hat{u}}{\mathrm{d}x},\frac{\mathrm{d}\phi}{\mathrm{d}x}\right)+\lambda^2(\hat{u},\phi)\right\}-\left(\hat{p},\frac{\mathrm{d}\phi}{\mathrm{d}x},\right)=(\hat{f}^{(1)},\phi),$$

$$\mu\left\{\left(\frac{\mathrm{d}\hat{v}}{\mathrm{d}x},\frac{\mathrm{d}\phi}{\mathrm{d}x}\right)+\lambda^2(\hat{v},\phi)\right\}+\mathrm{i}\beta k\left(\hat{p},\phi\right)=(\hat{f}^{(2)},\phi),$$

$$\mu\left\{\left(\frac{\mathrm{d}\hat{w}}{\mathrm{d}x},\frac{\mathrm{d}\phi}{\mathrm{d}x}\right)+\lambda^2(\hat{w},\phi)\right\}+\mathrm{i}\beta l\left(\hat{p},\phi\right)=(\hat{f}^{(3)},\phi)$$

for all $\phi\in X$, and

$$-\left(\frac{\mathrm{d}\hat{u}}{\mathrm{d}x}+\mathrm{i}\beta k\hat{v}+\mathrm{i}\beta l\hat{w},q\right)=0$$

for all $q\in M$, where X and M are chosen to be

$$X=\mathscr{H}^1_0((0,L_x)),$$

$$M=\mathscr{L}^2_0((0,L_x))$$

so that the solutions are well posed [15]. Here $\mathscr{H}^1_0((0,L_x))$ is the space of all functions that are square integrable on $(0,L_x)$, whose derivatives are square integrable, and that satisfy the Dirichlet boundary conditions at $x=0,L_x$. $\mathscr{L}^2_0((0,L_x))$ is the space of square integrable functions on $(0,L_x)$ with zero average.

Following Rønquist [41], we discretize these equations using spectral elements. Due to the coupling between the velocity and pressure, we may not discretize them independently: to avoid spurious modes we must choose compatible subspaces. For a discussion of the necessary conditions of compatibility see [5]. We split our domain $(0,L_x)$ into K equal elements, and choose the following subspaces that exclude parasitic modes:

$$X_h = \mathscr{H}_0^1((0,L_x)) \cap \mathscr{P}_{N,K}((0,L_x)),$$
$$M_h = \mathscr{L}_0^2((0,L_x)) \cap \mathscr{P}_{N-2,K}((0,L_x)),$$

where $\mathscr{P}_{N-2,K}((0,L_x))$ is the space of polynomials of degree less than or equal to N restricted to the K elements. Our choice of bases for these spaces corresponds to a discretization of the velocity using N Gauss–Lobatto–Legendre points on each element and the pressure using $N-2$ Gauss–Legendre points. In this way, we are able impose the Dirichlet boundary conditions and preserve continuity of velocity between each element, but there are no boundary conditions on the pressure, and it may be discontinuous from element to element.

We use the Uzawa algorithm, as described in [28,36] to solve for the flow. The resulting matrix vector systems are solved using preconditioned conjugate gradient (PCG) methods. The preconditioner for the pressure equation is the diagonal Gauss–Legendre mass matrix (associated with the pressure discretization). The PCG residual corresponds to the discrete divergence of the velocity field, $-\mathbf{Du}$, and thus the specified convergence tolerance level reflects the degree to which the flow is incompressible. The spectrum of the preconditioned pressure operator is analyzed in [36]. In our implementation, for each given wavevector (k,l), the PCG pressure iteration typically converges within three iterations, as long as the spectral element resolution is high enough, which is consistent with Maday et al.'s results for semiperiodic problems.

The solution of the velocity equations involves the inversion of a Helmholtz operator. This is accomplished via PCG iteration with the inverse of the diagonal of the Helmholtz operator as preconditioner. This form of preconditioner is chosen since it is particularly easy to calculate. The condition number of the operator varies with wavenumber. In particle simulations, the lowest wavenumbers require the most iterations for convergence.

Further details of the code and its validation (including spectral convergence tests) are given in Dance [9].

Appendix D. γ^{FCM} functions

The γ^{FCM} functions, defined in Eqs. (20) and (24) can be calculated using empirical data from FCM simulations and carrying out a curve fitting procedure, to give γ^{FCM} in polynomial form:

$$a_0 + a_1\epsilon + a_2\epsilon^2.$$

The values of a_i given here were calculated using MATLAB's function *polyfit* for data such that $\epsilon \leqslant 0.1$, which fits the data in a least-squares sense. They are given in the following table.

γ^{FCM} functions

Model	Component	a_0	a_1	a_2
Particle–wall functions				
FCM-M	1	4.3912	−5.8639	6.2752
FCM-M	2	1.9275	−1.2935	1.2968
FCM-MD	1	7.7338	−21.6693	37.5721
FCM-MD	2	2.2147	−2.6269	4.5880
Particle–particle functions				
FCM-M	1	2.7253	−1.4872	0.7579
FCM-M	2	1.7367	−0.6973	0.4670
FCM-MD	1	4.0699	−4.9662	3.8485
FCM-MD	2	1.7597	−0.7747	0.5565

FCM-M refers to the monopole only version of the model and FCM-MD refers to the version using both monopole and dipole multipoles. Recall that component 1 is for a squeezing configuration: either a particle sedimenting towards a wall, or a pair of particles with equal and opposite forces along their line of centers. Component 2 is for a shearing flow: either a particle with an imposed force parallel to a wall, or a pair of particles with equal and opposite imposed forces orthogonal to their line of centers. We need not give component 3 since it has the same form as component 2.

References

[1] M.P. Allen, D.J. Tildesley, Computer Simulation of Liquids, Oxford University Press, Oxford, 1994.
[2] G.K. Batchelor, Brownian diffusion of particles with hydrodynamic interaction, J. Fluid Mech. 74 (1976) 1–29.
[3] J.F. Brady, G. Bossis, Stokesian Dynamics, Ann. Rev. Fluid Mech. 20 (1988) 111–157.
[4] H. Brenner, The slow motion of a sphere through a viscous fluid towards a plane surface, Chem. Eng. Sci. 16 (1961) 242–251.
[5] C. Canuto, Spectral Methods in Fluid Dynamics, Springer, Berlin, 1988.
[6] E. Climent, M.R. Maxey, Numerical simulations of random suspensions at finite Reynolds numbers, Int. J. Multiphase Flow 29 (4) (2003) 579–601.
[7] M.D.A. Cooley, M.E. O'Neill, On the slow rotation of a sphere about a diameter parallel to a nearby plane wall, J. Inst. Math. Appl. 4 (1968) 163–173.
[8] M.D.A. Cooley, M.E. O'Neill, On the slow motion generated in a viscous fluid by the approach of a sphere to a plane wall or stationary sphere, Mathematika 16 (1969) 37–49.
[9] S.L. Dance, Particle sedimentation in viscous fluids, Ph.D. Thesis, Brown University, 2002.
[10] D.I. Dratler, W.R. Schowalter, Dynamic simulation of suspensions of non-Brownian hard spheres, J. Fluid Mech. 325 (1996) 53–77.
[11] A.L. Fogelson, C.S. Peskin, A fast numerical method for solving the three-dimensional Stokes equations in the presence of suspended particles, J. Comput. Phys. 79 (1988) 50–69.
[12] P. Ganatos, R. Pfeffer, S. Weinbaum, A numerical solution technique for three-dimensional Stokes flows, with application to the motion of strongly interacting spheres in a plane, J. Fluid Mech. 84 (1978) 79–111.
[13] P. Ganatos, S. Weinbaum, R. Pfeffer, A strong interaction theory for the creeping motion of a sphere between plane parallel boundaries. Part 1. Perpendicular motion, J. Fluid Mech. 99 (4) (1980) 739–753.
[14] P. Ganatos, S. Weinbaum, R. Pfeffer, A strong interaction theory for the creeping motion of a sphere between plane parallel boundaries. Part 2. Parallel motion, J. Fluid Mech. 99 (4) (1980) 755–783.
[15] V. Girault, P.-A. Raviart, Finite Element Methods for Navier–Stokes Equations: Theory and Algorithms, Springer, Berlin, 1986.
[16] R. Glowinski, T.W. Pan, T.I. Hesla, D.D. Joseph, J. Périaux, A fictitious domain approach to the direct numerical simulation of incompressible viscous flow past moving bodies: application to particulate flow, J. Comput. Phys. 169 (2001) 363–426.
[17] A.J. Goldman, R.G. Cox, H. Brenner, Slow viscous motion of a sphere parallel to a plane wall – I Motion through a quiescent fluid, Chem. Eng. Sci. 22 (1967) 637–651.
[18] P. Gondret, E. Hallouin, M. Lance, L. Petit, Experiments on the motion of a solid sphere toward a wall: from viscous dissipation to elastohydrodynamic bouncing, Phys. Fluids 11 (9) (1999) 2803–2805.
[19] H.H. Hu, Direct simulation of flows of solid–liquid mixtures, Int. J. Multiphase Flow 22 (2) (1996) 332–335.
[20] K. Ichiki, Improvement of the Stokesian Dynamics method for systems with a finite number of particles, J. Fluid Mech. 452 (2002) 231–262.
[21] K. Ichiki, J.F. Brady, Many-body effects and matrix inversion in low-Reynolds number hydrodynamics, Phys. Fluids 13 (1) (2001).
[22] M.S. Ingber, Dynamic simulation of the hydrodynamic interaction among immersed particles in Stokes flow, Int. J. Numer. Methods Fluids 10 (1990) 791.
[23] D.J. Jeffrey, Low Reynolds number flow between converging spheres, Mathematika 29 (1982) 58–66.
[24] D.J. Jeffrey, Y. Onishi, Calculation of the resistance and mobility functions for two unequal rigid spheres in low-Re flow, J. Fluid Mech. 139 (1984) 261–290.
[25] D.J. Jeffrey, Y. Onishi, The forces and couples acting on two nearly touching spheres in low-Reynolds-number flow, Zeit. angew. Math. Phys. 35 (1984) 634–641.
[26] G.B. Jeffrey, On the steady rotation of a solid of revolution in a viscous fluid, Proc. Lond. Math. Soc. 2 (14) (1915) 327–338.
[27] A.A. Johnson, T.E. Tezduyar, Simulation of multiple spheres in a liquid-filled tube, Comput. Methods Appl. Mech. Engrg. (1996) 351–373.

[28] G.E. Karniadakis, S.J. Sherwin, Spectral/hp Element Methods for CFD, Oxford University Press, Oxford, 1999.
[29] S. Kim, S.J. Karrila, Microhydrodynamics: Principles and Selected Applications, Butterworth–Heinemann, London, 1991.
[30] A.J.C. Ladd, R. Verberg, Lattice–Boltzmann simulations of particle–fluid suspensions, J. Stat. Phys. 104 (2001) 1191–1251.
[31] D. Liu. 2002, Personal communication.
[32] D. Liu, M.R. Maxey, G.E. Karniadakis, A fast method for particulate microflows, J. MEMS 11 (6) (2002) 691–702.
[33] S. Lomholt, Numerical investigations of macroscopic particle dynamics in microflows, Ph.D. Thesis, Risø National Laboratory, Roskilde, Denmark, 2000.
[34] S. Lomholt, M.R. Maxey, Force coupling method for particulate two-phase flow: Stokes flow, J. Comput. Phys. 184 (2) (2003) 381–405.
[35] S. Lomholt, B. Stenum, M.R. Maxey, Experimental verification of the force coupling method for particulate flows, Int. J. Multiphase Flow 28 (2002) 225–246.
[36] Y. Maday, D. Meiron, A.T. Patera, E.M. Rønquist, Analysis of iterative problems for the steady and unsteady stokes problem: application to spectral element discretizations, SIAM J. Sci. Comput. 14 (2) (1993) 310–337.
[37] M.R. Maxey, B.K. Patel, Localized flow representations for particles sedimenting in Stokes flow, Int. J. Multiphase Flow 27 (9) (2001) 1603–1626.
[38] M.E. O'Neill, S.R. Majumdar, Asymmetrical slow viscous fluid motions cause by the translation or rotation of two spheres. Part I: the determination of exact solutions for any values of the ratio of the radii and separation parameters, Z. angew. Math. Phys. 21 (1970) 164–179.
[39] M.E. O'Neill, K. Stewartson, On the slow motion of a sphere parallel to a nearby plane wall, J. Fluid Mech. 27 (1967) 705–724.
[40] C. Pozrikidis, A spectral element method for particulate Stokes flow, J. Comput. Phys. 156 (1999) 360–381.
[41] E.M. Rønquist, Optimal spectral element methods for the unsteady three-dimensional incompressible Navier Stokes equations, Ph.D. Thesis, M.I.T., 1988.
[42] W.B. Russel, D.A. Saville, W.R. Schowalter, Colloidal Dispersions, Cambridge University Press, Cambridge, 1989.
[43] A.S. Sangani, G. Mo, An O(N) algorithm for Stokes and Laplace interactions of particles, Phys. Fluids 8 (8) (1996).
[44] A. Sierou, J.F. Brady, Accelerated Stokesian Dynamics simulations, J. Fluid Mech. 448 (2001) 115–146.
[45] M. Stimson, G.B. Jeffery, The motion of two spheres in a viscous fluid, Proc. R. Soc. Ser. A 111 (757) (1926) 110–116.
[46] D. Sulsky, J.U. Brackbill, A numerical method for suspension flow, J. Comput. Phys. 96 (1991) 339–368.
[47] S. Zeng, E.T. Kerns, R.H. Davis, The nature of particle contacts in sedimentation, Phys. Fluids 8 (6) (1996).